

Space-Charge-Limited Photocurrents and Transient Currents in (Cd,Zn)Te Radiation Detectors

Katarina Ridzonova^{✉,*}, Eduard Belas[✉], Roman Grill[✉], Jakub Pekarek[✉], and Petr Praus[✉]
Charles University, Faculty of Mathematics and Physics, Institute of Physics, Ke Karlovu 5, 121 16, Prague 2, Czech Republic

 (Received 12 February 2019; revised manuscript received 19 January 2020; accepted 22 May 2020; published 22 June 2020)

We combine steady-state photoconductivity and laser-induced transient current measurements under above-band-gap illumination to study space-charge formation in (Cd,Zn)Te. Analytical and numerical models describing space-charge-limited photocurrents are developed and excellent agreement with measured data is obtained, especially with the Drift-diffusion model. A linear rise of photocurrent at low voltage is observed and ascribed to the trapping of injected holes in the region close to the cathode side. The influence of space-charge formation, the influence of photoconductive gain, and the contribution of shallow and deep levels to photocurrent-voltage characteristics are numerically simulated. According to measurements and calculations, recent principles used to evaluate detector properties, mainly the mobility-lifetime product, via the photoconductivity are critically assessed.

DOI: [10.1103/PhysRevApplied.13.064054](https://doi.org/10.1103/PhysRevApplied.13.064054)

I. INTRODUCTION

The influence of space charge on charge transport, space-charge-limited currents (SCLCs), and the shape of current-voltage characteristics in semiconductors equipped with injecting contacts have been extensively studied for decades, since the pioneering works of Lampert [1] and Mott and Gurney [2]. An overview of recent examinations may be found, for example, in Ref. [3]. Materials are mostly investigated through the effect of space-charge buildup and respective screening of the electric field with the single-carrier formula, neglecting diffusion current:

$$J_{\text{SCLC}} = \frac{9}{8} \frac{\epsilon_0 \epsilon_r \mu_e \theta V^2}{L^3}, \quad (1)$$

where ϵ_0 , ϵ_r , μ_e , V , and L are the vacuum and relative permittivity, electron mobility, voltage, and thickness of the planar sample, respectively. Electron injection from the cathode dominating in the circuit is assumed. The material is characterized by the ratio of the free electron density, n , and the sum of the free and trapped electron density, n_t

$$\theta = \frac{n}{n + n_t}. \quad (2)$$

The free-to-trapped electron density ratio is calculated in nondegenerate Boltzmann statistics in the form

independent of the Fermi energy

$$\frac{n_t}{n} = \frac{g N_t}{N_C} e^{\frac{E_t}{k_B T}}, \quad (3)$$

where N_C , g , N_t , E_t , and T are the effective density of states in the conduction band, the degeneracy factor of the trap, the trap density, the depth of the trap relative to the conduction band, and the absolute temperature, respectively. Space charge stored in the trap usually dominates above the free electron charge and $\theta = n/n_t$ is routinely used. The properties of the dominant trap responsible for carrier trapping and space-charge formation are deduced by an Arrhenius-type fit combined with other techniques, such as photoinduced current transient spectroscopy and thermally stimulated current measurements [4,5].

The exploration of materials and devices by space-charge-limited photocurrents (SCLPs) offers a significantly wider set of experiments and representative data characterizing the investigated system than one could extract from SCLCs. Using the above-band-gap light absorbed in close proximity to the illuminated semitransparent electrical contact allows researchers to maintain a tunable source of carriers as a substitution of carriers supplied by the injection contact in SCLCs. The space charge may thus be created, regardless of the type of contact. In addition, variable excitation may be also used when investigating the dynamics of space-charge formation, with much better precision than could be arranged by voltage pulsing. Another option is connected with the investigation of the material and contact homogeneity by scanning selected contact regions. In contrast to the evident advantages, the

*katka.ridzonova@gmail.com

parallel creation of both electrons and holes and their trapping near the contact may affect their electrical properties, which could manifest in a variation of the dark-current component. Effects related to this entanglement should be considered in the analysis to eliminate possible faults in data evaluation.

Measurement of photocurrent-voltage characteristics (PV) at above-band-gap illumination has become a common method to evaluate important transport properties, such as the carrier mobility-lifetime product $\mu\tau$. The mostly used approach to fit the dependence of photocurrent J on internal electric field E is based on Eq. (4), attributed to Many [6], which, in the case of above-band-gap light illuminating the cathode, is

$$J = \frac{J_0}{1 + \frac{s_e}{\mu_e E}} \frac{\mu_e \tau_e E}{L} \left[1 - \exp\left(-\frac{L}{\mu_e \tau_e E}\right) \right]. \quad (4)$$

Here, J_0 represents the saturation photocurrent, which is proportional to the excitation intensity, and L is the thickness of a planar sample. The electron transport characteristics are described by mobility μ_e , lifetime τ_e , and surface recombination velocity s_e . Considering strong attenuation of the above-band-gap light absorbed typically at a depth of less than 1 μm near the surface, photogenerated holes are almost immediately drained by the cathode under an applied voltage, while electrons drift through the bulk to the anode. Thus, only electrons contribute to the overall photoconductivity and the problem is limited to the solution of a single-particle-type task. Analogously, the hole signal can be recorded by simply reversing the applied-voltage polarity or by irradiating the opposite contact. Other presumptions, in which Eq. (4) is valid, are suppressed carrier injection from surface states and spatially constant μ_e and τ_e . In the case of electrical contacts directly deposited on the sample's surface, ohmic-type contacts and flat bands at the metal-semiconductor interface should be maintained. It should be mentioned that the original derivation of Eq. (4) did not assume a steady-state voltage. Pulsed field and blocking electrodes detached from contacts by an insulating spacer were used. The key assumption for the validity of Eq. (4) is the spatially uniform internal electric field, $E = V/L$, for applied voltage V , which equals the clause of zero-space-charge distribution in the sample, either induced by nonohmic contacts or by photoexcitation.

Many's Eq. (4) is routinely used in the determination of $\mu\tau$ in various semiconductor materials, such as (Cd, Zn)Te [7–12], HgI₂ [13,14], Tl₄CdI₆ [15], (Sb, Se)I [16], TiSi₄ [17], Cs₂Hg₃S₄ [18], hexagonal boron nitride [19–23], halide perovskite CH₃NH₃PbI₃ [24], and CsPbBr₃ films [25]. However, in all cases, it is hard to deduce if the key assumption of a uniform electric field is fulfilled, since the measurement of the PV characteristics does not reveal the presence of space charge in the sample. If this requisite is

not met, another model involving the influence of space charge will have to be used [9,26,27] or an experiment should be set up to maintain a homogeneous electric field. Space charge can be reduced or fully prevented by using a chopped regime of illumination instead of continuous one, as it was done in Refs. [10,16–18,25,28]. Even under such experimental conditions, however, Eq. (4) should be used cautiously, as the space-charge relaxation can proceed with much slower dynamics than that of its formation, and a memory effect can also debase the results.

The laser-induced transient current technique (LTCT) represents, nowadays, a prospective tool for how to non-destructively investigate the bulk properties of semi-insulating materials with an extended lifetime of at least one of the photogenerated carriers [29]. A detailed analysis of the current waveform shape enables us to evaluate the drift mobility of carriers and their lifetime, as well as the electric field and space-charge profile along the sample thickness [30]. It may be thus used as an independent technique in the verification of theoretical predictions offered by the theory of SCLPs.

Here, we report on the theoretical and experimental investigation of SCLPs. We develop three photoconductivity models under above-band-gap illumination, which involve space-charge formation in addition to surface recombination. We also propose a method based on the LTCT, which allows us to clearly prove or refute the presence of space charge within the studied material. According to the results, one can decide whether the measured PV characteristics might be evaluated by Many's Eq. (4) or by models involving space charge. All measurements are performed on (Cd, Zn)Te with 15% zinc content, which is a suitable semiconductor material for the fabrication of room-temperature x-ray and gamma-ray detectors. It is distinguished by a relatively high atomic number, wide energy band gap (~ 1.5 eV), and high resistivity [31] at room temperature.

II. THEORY

A. Space-charge-limited photocurrents 1

In this section, we introduce the simplest analytical model to describe SCLPs, further denoted SCLP1. It is advantageous for the initial characterization of the most important processes occurring in a sample subjected to above-band-gap cathode illumination and ensuing space-charge formation. The model considers one shallow trap and neglects the dark currents and photogenerated holes.

The shallow trap allows us to use the nondegenerate Boltzmann statistics to define its occupancy. By neglecting the concentration of free electrons in the dark, n_0 , and trapped electrons, n_{t0} , relative to the photoexcited electrons, the space-charge density, ρ , may be expressed

as

$$\rho = -e(n - n_0 + n_t - n_{t0}) \cong -e\frac{n}{\theta} \quad (5)$$

where θ is defined in Eq. (2) and e is the elementary charge. Combining Eq. (5), Poisson's equation, and Ohm's law, in the same way that in the derivation of SCLCs from Eq. (1) [32], one may express the electric field dependence on spatial coordinate x , where $x=0$ corresponds to the illuminated cathode and $x=L$ corresponds to the anode, as

$$E(x) = -\sqrt{E^2(0) + \frac{2jx}{\epsilon_0\epsilon_r\mu_e\theta}}, \quad (6)$$

where j represents the current density.

The boundary condition represented by the electric field just below the illuminated contact, $E(x=0)$ in Eq. (6), may be obtained by solving the balanced equation describing the surface dynamic equilibrium between the incident light intensity I_l , surface recombination, and drift into the bulk

$$I_l - s_e n(0) - \frac{j}{e} = 0, \quad (7)$$

which yields

$$E(0) = -\frac{s_e j}{\mu_e(I_l e - j)}. \quad (8)$$

The term connected to the direct or deep-level-mediated interband recombination in the sample's bulk is omitted in Eq. (7) due to negligible dark currents. Since almost no free holes are present in the semiconductor volume, electrons cannot recombine there and we can assume an infinite carrier lifetime τ_e . With the aim of presenting the results in a form consistent with generally used visualizations, we define the electric current as positive overall herein, in spite of the negative electric field applied to the sample. Integrating Eq. (6) through sample thickness L , we may express the applied voltage V as being dependent on j :

$$V = \frac{\epsilon_0\epsilon_r\mu_e\theta}{3j} \left(\left(\left[\frac{s_e j}{\mu_e(I_l e - j)} \right]^2 + \frac{2jL}{\epsilon_0\epsilon_r\mu_e\theta} \right)^{3/2} - \left[\frac{s_e j}{\mu_e(I_l e - j)} \right]^3 \right). \quad (9)$$

When the drift term in Eq. (7) is much less than the other two terms, Eq. (9) may be converted into Eq. (1). Notably, Eq. (9) involves the steady-state current and does not contain any parameter defining the interaction of free electrons with the trap. Consequently, this model cannot be used for determining quantities that define electron (de)trapping,

such as the carrier capture cross section, lifetime, and the mobility-lifetime product. On comparing these findings with Many's Eq. (4), it is evident that the application of Eq. (4) to the steady-state experiment described by Eq. (9), in an effort to determine $\mu\tau$, is unsupported.

A formula similar to Eq. (9) was also derived by du Chatenier [26]. The main difference between du Chatenier's model and SCLP1 lies in the boundary condition represented by the electric field just below the illuminated contact, $E(x=0)$. du Chatenier's balanced Eq. (7), which is used in the derivation of the boundary condition, depicts surface recombination by the term n/τ_e [33]. This term is connected to the direct or deep-level-mediated interband recombination defined by the electron lifetime τ_e . Because both holes and electrons are generated by above-band-gap light absorbed in the region close to the surface, recombination here is possible. However, the term n/τ_e neglects completely the spatial dependence of the hole distribution and τ_e . In particular, it does not take into account a larger concentration of photogenerated holes close to the surface or a higher defect density at the surface, which both increase the recombination rate. Moreover, du Chatenier's balanced equation does not consider the drain of free carriers to the contact. As a consequence of these omissions, the quantity τ_e , appearing in du Chatenier's model, has only the physical meaning of mean lifetime at the surface, and it has no straight relation to the carrier lifetime in the bulk. Although it is noted in Ref. [26] that τ_e at the surface is considered, it is not accentuated there that τ_e cannot be used as the carrier lifetime in the bulk. Defining the boundary condition with the help of surface recombination s_e introduces a significant improvement into the SCLP1 model. In contrast to indeterminate τ_e , the parameter s_e corresponds to a well-defined quantity measurable by manifold techniques.

The SCPL1 model may also be easily generalized to a model of several shallow levels, if their occupancy is ruled by Boltzmann statistics. In such a case, the parameter θ may be obtained as

$$\theta = \frac{n}{n + \sum_i n_{ti}}, \quad (10)$$

where the summation runs over respective level occupancies n_{ti} and other terms remain unchanged.

1. Transient currents in the case of inhomogeneous space-charge distribution

The LTCT is a powerful tool for the investigation of principal electronic properties of semi-insulating materials, determining the electric field profile in semi-insulating semiconductors by analyzing the current waveform (CWF) shape [29,30,34–36]. It is common in (Cd,Zn)Te radiation detectors that the space charge is induced by blocking

contacts, ensuring a low dark current and carrier depletion. This setup leads to the formation of nearly constant space charge in the whole sample, unless a fully screened inactive region appears [30]. The CWF has an exponential dependence on time $I(t) \sim e^{-ct}$, where the damping factor, c , is related to the space charge and mobility-lifetime product $\mu_e \tau_e$ [37].

Conversely, for inhomogeneous space-charge density induced by injecting contacts or by above-band-gap illumination, we have to use Eqs. (6) and (8) to define the internal electric field. According to the Ramo theorem [38], the CWF induced by charge Q moving with velocity v through a planar sample of thickness L can be generally expressed as [37]

$$i(t) = \frac{Q(t)v(t)}{L}. \quad (11)$$

The trajectory of an electron excited at the cathode is easily calculated by integrating the kinetic equation $dx/dt = -\mu_e E(x)$, in which $E(x)$ and $E(0)$, defined by Eqs. (6) and (8), respectively, are used:

$$x(t) = \frac{\epsilon_0 \epsilon_r \mu_e \theta}{2j} \left[\left(\frac{jt}{\epsilon_0 \epsilon_r \theta} - E(0) \right)^2 - E^2(0) \right]. \quad (12)$$

Time derivation and substituting into Eq. (11) finally leads to CWF in the form

$$i(t) = \frac{Q(t)\mu_e}{L} \left(\frac{jt}{\epsilon_0 \epsilon_r \theta} - E(0) \right). \quad (13)$$

In the case of a good-quality sample, when the carrier lifetime significantly exceeds the time of the passing of carriers through the detector (called the transit time), time-independent $Q(t) = Q_0$ may be used and $i(t)$ attains a linear shape. As it results from Eq. (13), increasing transient current confirms the presence of a negative space charge in the detector, while the decreasing current shape after the onset corresponds to a positive space charge.

B. Space-charge-limited photocurrents 2

In the second model, called SCLP2, we generalize the previous model SCLP1. In addition to SCLP1, we assume the general energy of deep trapping levels, possibly located near the Fermi energy, in which the Fermi-Dirac statistics to define level occupancy, instead of Boltzmann statistics, must be used. In addition, we also consider a substantial density of free electrons supplied by the ohmic cathode. By integrating the Gauss' law, we obtain the following

transcendental equation for internal electric field:

$$\begin{aligned} -A[E(x) - E(0)] + B \ln \left| \frac{E(x) - E_1}{E(0) - E_1} \right| + C \ln \left| \frac{E(x) - E_2}{E(0) - E_2} \right| \\ = \frac{e}{\epsilon_0 \epsilon_r} ADx. \end{aligned} \quad (14)$$

A detailed derivation of Eq. (14), corresponding to the SCLP2 model, and the meaning of individual parameters A, B, C, D, E_1, E_2 , and $E(0)$ can be found in the Appendix. The electric field profile $E(x)$ is calculated numerically for each $x \in (0, L)$ and fixed trap parameters are obtained by solving Eq. (14) with a given j , which is obtained from experiments. The respective voltage V is acquired by the integration of $E(x)$. The whole PV dependency is obtained by repeating the procedure with different j . Similarly, as in the case of SCLP1, we see that SCLP2 does not involve any parameter that defines (de)trapping or the carrier lifetime. Electrons may leave the sample only at contacts, by surface recombination at the cathode and by the drain at the anode.

C. Drift-diffusion model

Analytical models SCLP1 and SCLP2 are based on a significant simplification, which could make them useless under general conditions and render the obtained results inaccurate. Especially neglected is the contribution of holes, which may affect the transport characteristics in the high-resistivity n -type samples and even more markedly in p -type samples. The involvement of holes in the calculations disables the utilization of an analytical approach and a fully numerical treatment must be engaged. We adopt, for this purpose, previous codes for the simulation of transient currents to solve, in parallel, drift-diffusion and Poisson's equations in a material with traps [39]. In addition, we refine the boundary condition to define the interface carrier density by involving an interface layer, which suppresses surface recombination. Instead of a fixed free-carrier density directly defined by the metal-semiconductor Schottky barrier, we use a dynamic prescription according to Refs. [40,41] and define the free-carrier current at the electrodes in the form

$$J_e(0) = -\gamma_e^{(0)} e [n_0^{(0)} - n(0)], \quad (15a)$$

$$J_h(0) = \gamma_h^{(0)} e [p_0^{(0)} - p(0)], \quad (15b)$$

$$J_e(L) = \gamma_e^{(L)} e [n_0^{(L)} - n(L)], \quad (15c)$$

$$J_h(L) = -\gamma_h^{(L)} e [p_0^{(L)} - p(L)], \quad (15d)$$

where $J_{e(h)}(0)$, $n_0(p_0)^{(0)}$, $J_{e(h)}(L)$, and $n_0(p_0)^{(L)}$ are the equilibrium electron (hole) current density and dark density of electrons and holes at the cathode ($x=0$) and anode ($x=L$), respectively. Respective γ factors define the transfer rate through the interface. In addition to Refs. [40,41], where only limiting cases $\gamma=0$ and $\gamma=\infty$ were considered, we use a general γ in the fit of experimental data. Notably, $n_0(p_0)$ may be different at the cathode and anode due to possibly unlike band bending at interfaces.

An improvement of the contact model is indispensable for the correct description of the current in a biased sample and surface recombination under illumination. The case with $\gamma=0$ suppresses surface recombination by the draining of the respective carrier to the contact. Simultaneously, it completely disables the electric current. Conversely, $\gamma=\infty$ induces a large surface recombination of carriers excited by the above-band-gap light in the thin layer ($<1\ \mu\text{m}$) below the semitransparent contact. We apply the contact model to define the interface transfer of carriers by the linear functions of the carrier density, Eqs. (15a)–(15d), for a description of the basic properties of the current-carrying illuminated interface with a general value of the γ factor.

Drift-diffusion electron and hole equations [39] involving carrier (de)trapping on defect levels, as described by the Shockley-Read-Hall model, are numerically time-integrated. Adaptive step-size control of the fourth-order Runge-Kutta method is used for integration. The electrostatic potential and electric field profile are calculated by solving the Poisson's equation at each integration step. Simulation of the steady-state and chopped photoconductivity occurring in the period significantly exceeding the drift time or lifetime of free carriers is done with electrons and holes in a steady-state distribution. This simplification does not notably disturb the obtained results, but it significantly speeds up the calculation and allows us to make simulations in a reasonably short time period, without putting big demands on the computational resources [39].

The analytical model described in this section is referred to hereafter as the drift-diffusion model (DDF).

III. EXPERIMENT

All measurements are performed on an *n*-type semi-insulating $\text{Cd}_{0.9}\text{Zn}_{0.1}\text{Te}$ sample, further denoted as *A*, which is grown by the high-pressure Bridgman growth method. In addition, seven other samples grown by the traveling heater method (THM) and high-pressure Bridgman growth method, not shown in this paper, are measured. All samples reveal similar behavior to that observed on the presented sample.

Sample *A* is mechanically polished by SiC abrasive and chemically etched in 3% bromine-methanol solution

1 min, after which time it is rinsed in methanol and isopropyl alcohol. Gold contacts are deposited from 1% aqueous solution of AuCl_3 onto both largest sides of the sample, with dimensions $6 \times 4 \times 1.4\ \text{mm}^3$. The electron mobility-lifetime product of sample *A*, as determined by alpha spectroscopy, is $1.2 \times 10^{-3}\ \text{cm}^2\ \text{V}^{-1}$ and its resistivity is $7.6 \times 10^{10}\ \Omega\ \text{cm}$.

PV characteristics under continuous illumination are measured by a laser diode powered by a Tektronix AFG 3252 arbitrary waveform generator. The wavelength of incident light is 690 nm ($h\nu \approx 1.87\ \text{eV}$) with an intensity of $4\ \mu\text{W}/\text{cm}^2$. A homogeneously irradiated area of $3\ \text{mm}^2$ is used as a compromise between homogenous illumination of the whole sample and an effort not to illuminate edges of the sample. A smaller illumination spot could lead to lateral broadening of the current due to diffusion, and the one-dimensional (1D) approximation used in our theoretical models may not be sufficient. To probe local properties with a small illumination spot, one should use a three-dimensional model instead of 1D approximation. Current through the sample is measured indirectly on a $1\ \text{M}\Omega$ load resistor. Since we irradiate the cathode side of the samples with above-band-gap light, only electrons contribute to the measured signal. The final photocurrent is determined as the difference between the current under illumination and dark current. In this way, the leakage current is extracted from the measurements and does not influence presented data. During illumination of the sample, we are also careful not to illuminate edges of the sample, so extra leakage current is not induced by the light.

Laser-induced transient currents using dc voltage [34] are excited from the cathode side by probing laser pulses with 2 ns width, 100 Hz repetition frequency, and above-band-gap 662 nm wavelength (see Fig. 1). Acquired CWFs are amplified by a high-frequency bipolar 3-GHz Miteq AM-1607-3000R amplifier, with a signal conversion of $6.85\ \text{mV}/\mu\text{A}$ into a voltage pulse, and then are recorded using a 4-GHz digital LeCroy oscilloscope [42] on the $50\ \Omega$ dc input resistance. The laser pulse intensity and repetition frequency are tested to be low enough, so that the photocurrent and current waveform shape are not influenced by the laser pulses.

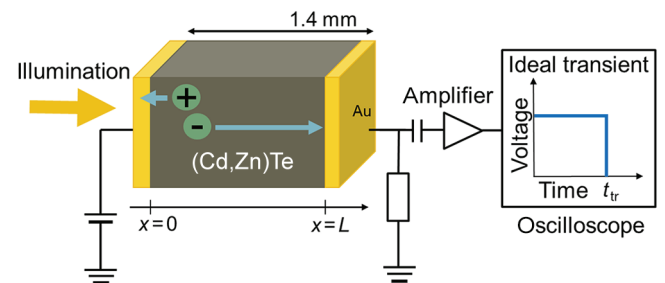


FIG. 1. Scheme of LTCT measurement.

IV. RESULTS AND DISCUSSION

A. Photocurrent

To compare the theoretical models, we measure PV characteristics under a continuous regime of cathode illumination. Experimental data for sample *A*, together with fits by Many's equation, the SCLP1 model, and DDF model, are shown in Fig. 2. We can see that the measured photocurrent versus voltage curve may be split into regions of nearly linear rise up to a voltage of about 200 V with saturation above 200 V. In the linear region, the space charge induced by photoelectrons captured in bulk trap levels significantly screens the voltage near the cathode, and part of the photoelectrons may pass to the anode, while many disappear near the cathode due to surface recombination. At photocurrent saturation, screening of the electric field near the cathode is suppressed and most of the photoelectrons are collected. The maximum photocurrent at saturation is obviously limited by the intensity of illumination, $j = eI_l$. In some samples, the saturation part of the photocurrent can be tilted due to contact effects, mainly by photoconductive gain caused by a large space charge formed by trapped photoholes near the cathode [43]. We observe such an effect in several of our samples. Chosen sample *A* does not show such an effect and the saturation is well defined.

Comparing the fit to Many's equation with that of the SCLP1 model, we clearly observe much better agreement of the SCLP1 model with experimental data. Similar discord of the fit to Many's equation with experimental data is also identified in previous studies [8,9]. Fit parameters

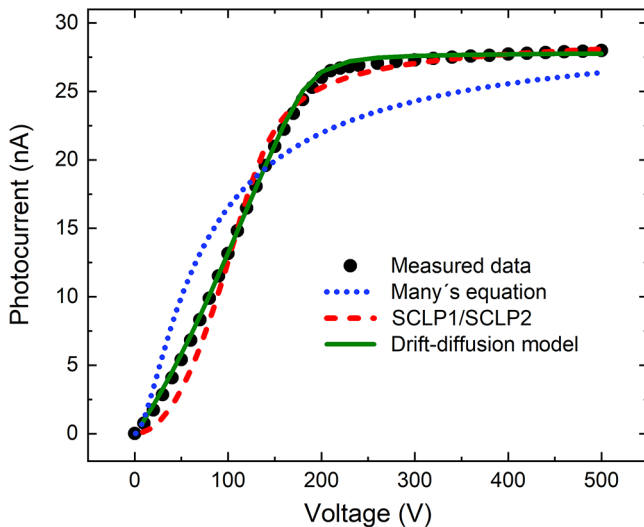


FIG. 2. PV characteristics of sample *A* gained under continuous laser diode illumination with a wavelength of 690 nm, measured in the configuration for collecting electrons only. Measured data are fitted according to Many's equation (dotted line), SCLP1/SCLP2 models (dashed line), and DDF model (green line).

obtained from Many's equation are $s_e/\mu_e = 140 \text{ V cm}^{-1}$ and $\mu_e\tau_e = 2.3 \times 10^{-4} \text{ cm}^2 \text{ V}^{-1}$, which is a value 5 times lower than that of $\mu_e\tau_e$ obtained from alpha spectroscopy.

Fitting with the SCLP1 model under the assumption of fixed mobility, $\mu_e = 1057 \text{ cm}^2 \text{ V}^{-1} \text{ s}^{-1}$ for (Cd,Zn)Te [39] gives a surface recombination velocity of $s_e = 170\,000 \text{ cm s}^{-1}$ and $\theta = 5 \times 10^{-5}$. The SCLP2 model, considering an experimentally determined value of $n_0 = 7.8 \times 10^4 \text{ cm}^{-3}$, leads to an almost identical fit to that with the SCLP1 model, since the best results for sample *A* are obtained in the presence of a shallow trap with $E_t < 0.54 \text{ eV}$ at which both models coincide.

For the explicit illustration of the effect of various parameters on the photocurrent, we plot in Fig. 3 the SCLP1 fit together with curves obtained upon changing parameters θ , I_l , and s_e . Initial fitting of parameters corresponding to the black curve remain the same as those in Fig. 2. In the case of reduced θ , greater screening of the electric field induced by the respective deep level implies a slower onset of the PV characteristics and delayed saturation. Reduced I_l is represented by a correspondingly reduced saturation current. Increased s_e makes the transfer between increasing and saturated parts of the PV characteristics more gradual, and the curve is similar to that obtained by fitting to Many's equation. It is seen that the parabolic shape of the PV characteristics at low voltages persists in all situations.

An illustration of the difference between the SCLP1 and SCLP2 models is shown in Fig. 4, where the degenerate Fermi-Dirac statistics are enforced in the SCLP2 model, with $n_1 = n_0$. The parameters of the SCLP1 model remain the same as those for the black curve

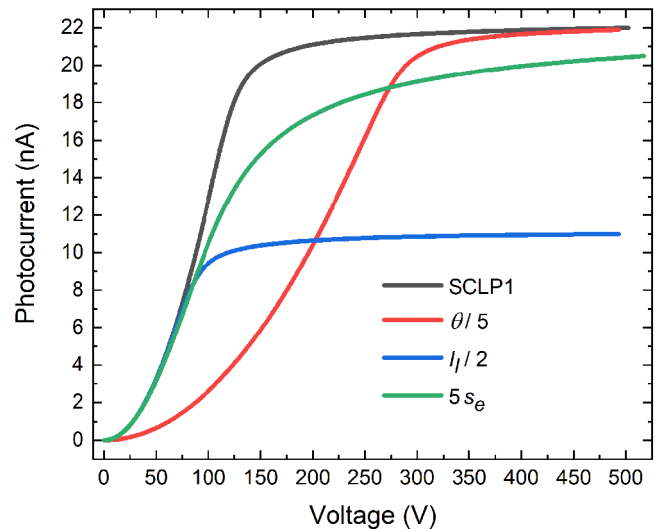


FIG. 3. Influence of changes in θ (red line), light intensity I_l (blue line), and surface recombination velocity s_e (green line) on the shape of PV characteristics (black line) calculated by the SCLP1 model.

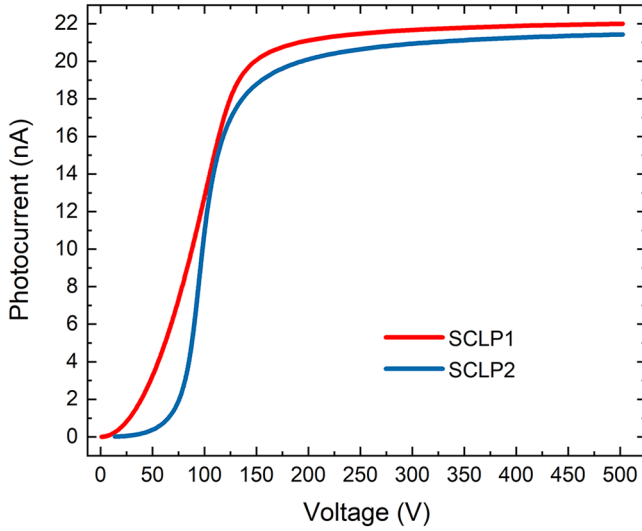


FIG. 4. Comparison of SCLP1 model (red line) and SCLP2 model with defect levels in Fermi energy (blue line).

in Fig. 3, while the parameters for the SCLP2 model are $\theta = 7 \times 10^{-7}$, $s_e = 170\,000 \text{ cm s}^{-1}$, $I_l = 2.6 \times 10^{12} \text{ cm}^{-2} \text{ s}^{-1}$, and $n_1 = n_0 = 7.8 \times 10^4 \text{ cm}^{-3}$. It is seen that degenerate-level occupancy results in an even slower photocurrent rise, which corresponds to a larger polynomial exponent than that of the second power resulting in SCLP1. Such a slow photocurrent rise, related to the presence of a deep level, is observed in Ref. [7]. From the shape of PV rise at low voltages presented in Fig. 4, one can estimate whether shallow or deep levels prevail in the material. The accuracy of the estimation may be, however, limited by the participation of holes in space-charge formation.

Although the SCLP1 and SCLP2 models fit the experimental data in Fig. 2 well, we see a distinct deviation, mainly at low bias in the region of incomplete carrier collection, manifesting in the convex bending of the SCLP curves. The measured photocurrent has a linear behavior, rather than the parabolic shape of the SCLP models. This deviation is interpreted as a consequence of simplifications used in the derivation of the SCLP models. Based on this consideration, we engage the DDF model described in Sec. II C to search for convenient defect and contact properties, which describe experimental data and are consistent with the mobility-lifetime product determined from alpha-spectroscopy.

In Fig. 5, we can see the measurement of PV characteristics at three different excitation intensities (4, 2.3, and $1.4 \mu\text{W}/\text{cm}^2$), along with a fit according to the DDF model, in which three defect levels and flat bands at the metal-semiconductor interface are assumed. The levels are characterized by concentration N_t , energy E_t , and capture cross sections of electrons and holes (σ_e and σ_h , respectively), as listed in Table I.

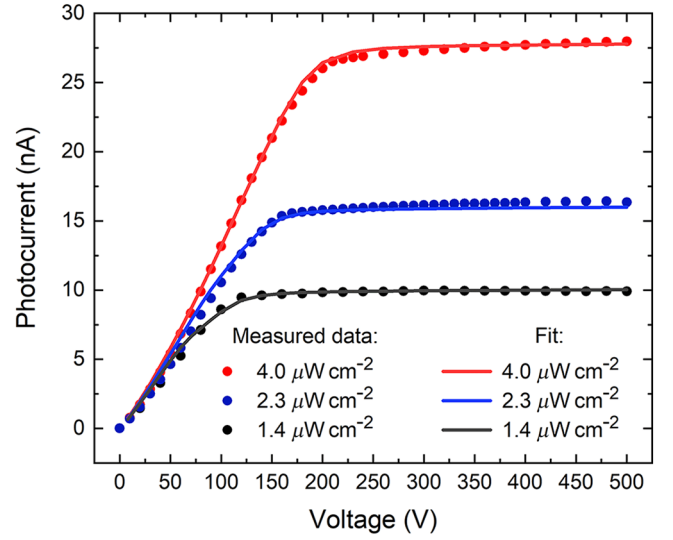


FIG. 5. PV characteristics measured on sample *A* at different light intensities with a wavelength of 690 nm. Measured data are fitted according to the DDF model with parameters listed in Table I.

Energy levels 1 and 2 are important in fitting of the photoconductivity, while level 3 is added to fit the appropriate lifetime evaluated from alpha spectroscopy. The position of the Fermi energy (E_F) used in the DDF model is set to the midgap region 0.76 eV below the conduction band. This chosen E_F is consistent with the measured resistivity of the material. Other material parameters are the band-gap energy, $E_g = 1.57 \text{ eV}$ [31], and the hole mobility, $\mu_h = 77 \text{ cm}^2 \text{ V s}^{-1}$ [44]. The absorption coefficient corresponding to a photon energy of 1.87 eV is deduced, according to Ref. [45], to be $\alpha = 25\,000 \text{ cm}^{-1}$. The transfer rate that defines the transfer of electrons through the cathode, $\gamma_e^{(0)} = 5 \times 10^4 \text{ cm s}^{-1}$, is obtained from the fit. Other transfer rates, $\gamma_h^{(0)}$, $\gamma_e^{(L)}$, and $\gamma_e^{(0)}$, do not influence the fit markedly and they are not fitted. They are fixed at a high value of 10^7 cm s^{-1} , which affords the surface density of respective free carriers defined directly by the Schottky barrier.

Important characteristics of the fit are outlined in Fig. 6, where the electric field and space-charge density [(Fig. 6(a)], level occupancy [Fig. 6(b)], and free carrier density [Fig. 6(c)] profiles calculated at 30 V are shown.

TABLE I. Fitting parameters of defect levels obtained using the DDF model to describe experimental data plotted in Figs 2, 5, and 7.

Energy level	$N_t(\text{cm}^{-3})$	$E_t(\text{eV})$	$\sigma_e(\text{cm}^2)$	$\sigma_h(\text{cm}^2)$
1	3×10^{11}	0.66	2×10^{-14}	1.0×10^{-14}
2	9×10^{11}	0.85	3×10^{-16}	2.5×10^{-15}
3	2×10^{12}	0.50	1×10^{-14}	0

Photoexcited electrons are primarily trapped on level 1, forming a negative space charge in the bulk of the sample. As a consequence, the electric field is screened near the cathode and increases towards the anode, which is depicted as a red line in Fig. 6(a).

The important feature, distinct from the predictions of SCLP models, is the shoulder clearly seen at $x \approx 0.05$ cm in all profiles. The reason for this artefact lies in the injection of holes from the anode and their participation in space-charge formation. While the hole density is low in the region $x \in (0.5, 1.4)$ mm due to a higher electric field, it increases near the cathode for $x < 0.5$ mm due to the lowered electric field. Consequently, enhanced hole trapping close to the cathode, mainly on level 2, results in a significant compensation of the negative space charge formed by photogenerated electrons in the sample. The width of this compensated region is dependent on the applied voltage and is enlarged with decreasing voltage. Since the deep electron trap, level 1, is significantly filled by trapped electrons, the free-electron lifetime increases and electrons may pass through the compensated region without undergoing strong trapping or recombination. The photocurrent then exceeds the paraboliclike theoretical prediction of the SCLP models and attains a nearly linear shape at low voltages. Linear growth of the photocurrent at low voltages observed in other studies [8–11,19–22] may also be assigned to the above-described phenomenon, in which injected holes from the anode participate in charge transport. In the case of a nonsaturated photocurrent, interpretation of the PV characteristics by strong surface recombination should be considered as well.

The positive space charge formed close to the cathode up to a depth of $x \sim 3 \mu\text{m}$ [Figs. 6(a) and 6(b)] is caused by the trapping of photoexcited holes on level 2. This effect results in an enhancement of the electric field near the cathode and increases the injection of electrons from the contact. In investigated sample *A*, injecting electrons are significantly damped by the low transfer rate, $\gamma_e^{(0)}$. A larger value of $\gamma_e^{(0)}$ would lead to an enhanced photoconductive gain [43] and no saturated photocurrent would be seen.

Although the number of parameters defining the fit appears to be large, a simplification of the model and a reduction of the number of parameters, for example, by joining levels 1 and 2 to an appropriate single level, is not successful. It is also worth mentioning that a similar model with two midgap levels is successfully applied to explain depolarization of the (Cd,Zn)Te radiation detector by the above-band-gap light [46]. Summarizing, the presented model with two levels positioned near the Fermi energy and another shallower electron trap conveniently depicts important features of the charge dynamics in the sample and consistently complies with all experimental results.

The DDF model can also be conveniently used for more complex situations if the nonuniform defect distribution

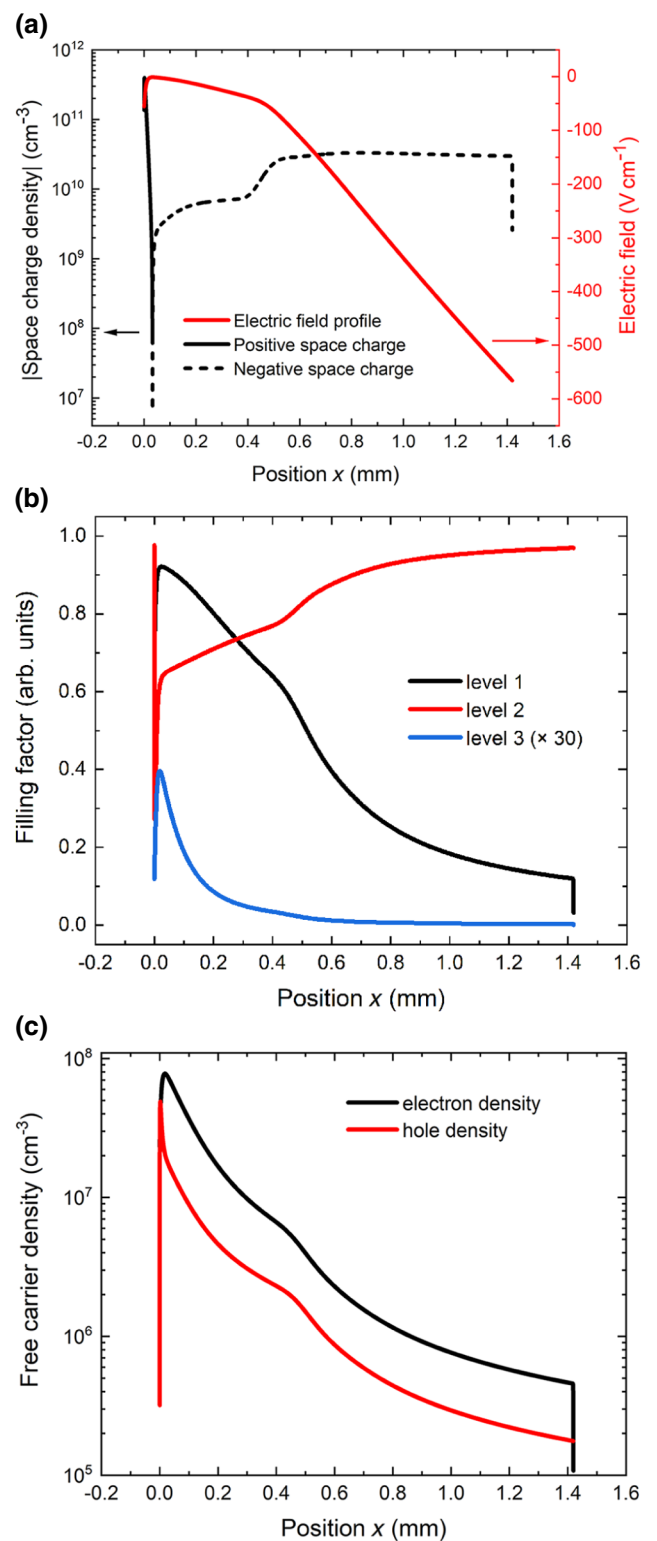


FIG. 6. (a) Absolute value of space-charge density normalized by elementary charge and electric field profile. (b) Profile of the occupancy of defect levels defined in Table I (blue line is multiplied by a factor of 30). (c) Profile of free electron and hole densities calculated by the DDF model at 30 V and an illumination intensity of $2.3 \mu\text{W cm}^{-2}$ with fit parameters listed in Table I.

induced, for example, by annealing or nonstandard surface treatment, is present. If such samples are investigated, theoretical predictions may be verified by the LTCT, which provides an extensive set of experimental results.

For practical application of Cd-Te-based materials, PV measurements performed under anode illumination are important, as one of the main drawbacks of (Cd,Zn)Te radiation detectors lies in the presence of hole traps and inconvenient hole collection. We also perform such an experiment. Our preliminary results show that the anode-illuminated PV reveals a significantly smaller signal than that of the cathode-illuminated PV, and photocurrent saturation is barely detected. This observation clearly proves that the hole trap critically affects the hole current, and the hole trap may be effectively investigated in this way.

B. Transient current measurements

We further compare the LTCT signal of sample *A* measured both in the dark and under steady-state cathode illumination to prove the existence of space charge in $\text{Cd}_{0.9}\text{Zn}_{0.1}\text{Te}$.

First, we illuminate only the cathode of the sample by probing laser pulses. The laser intensity and frequency are low enough that illumination does not influence the properties of the sample, but serve only for the characterization of the internal electric field. The formation of space charge originating from trapped photogenerated carriers is, in this case, eliminated. Examples of CWFs collected at different voltages of 30, 100, and 300 V are plotted in Figs. 7(a)–7(c), respectively, as black curves labeled “without LED.” Dotted lines represent the fit using the DDF model with parameters listed in Table I. The descending CWF apparent at all voltages is dominantly induced by the finite electron lifetime of $\tau_e = 1.2 \mu\text{s}$. The same τ_e is also derived from alpha-spectroscopy measurements and it is consistent with fitting parameters defining defect level 3. The descending CWF at 30 V has a higher damping factor c than that explained only by the value of $\mu\tau$ determined, which proves weak positive charging of the biased sample [37]. The positive space charge appearing in this setup can be created by variation of the carrier density induced by slightly blocking the cathode or injecting anode gold contacts. Such an effect is observed hourly in $\text{Au}/n\text{-(Cd,Zn)Te}/\text{Au}$ radiation detectors [29]. Weak undulations in the waveforms are partly caused by sample inhomogeneity and by the electronics used [29].

In the second regime, the cathode is simultaneously illuminated by the above-described probing pulses and by a continuous LED diode with a wavelength of 690 nm. In this case, we simulate the conditions that occur in the sample during continuous photocurrent measurements. Since the LTCT records only deviations from the steady state, the generated greater amount of charge carriers in the case of additional continuous illumination should not contribute

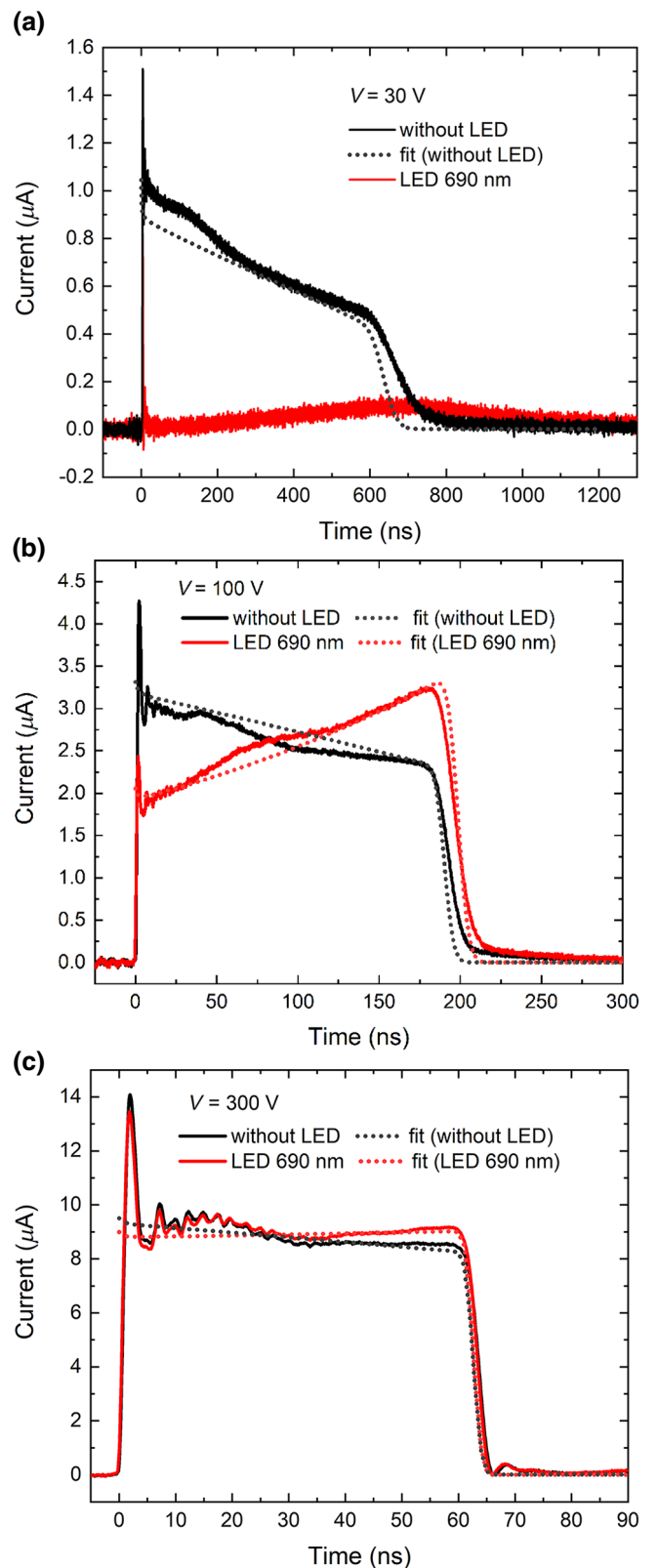


FIG. 7. Current waveforms measured on sample *A* by LTCT using only laser pulses (red line) and with additional continuous light-emitting diode (LED) illumination at 690 nm (black line) for (a) 30, (b) 100, and (c) 300 V. Dotted lines represent the fit using DDF model with parameters listed in Table I.

to the total current pulse. The principal effect of cathode illumination on the transient current profile is clearly demonstrated in Figs. 7(a)–7(c) by the red waveforms labeled “LED 690 nm.” The variations of CWFs under steady-state cathode illumination are caused by warping of the electric field induced by the negative space charge appearing due to the photocarrier trapping. The significantly suppressed electric field at low bias results in strong surface recombination and reduced collected charge. This phenomenon can be seen in Fig. 7(a), since the area under the CWF corresponds to the collected charge. By increasing the voltage, the electric field near the cathode grows in parallel as screening fades away, surface recombination is attenuated, and the waveforms attain their undisturbed shape, as it is apparent in Fig. 7(c). The crossing between a screened and unscreened cathode is ideally illustrated by the CWF in Fig. 7(b), where the waveform, although significantly tilted, reveals features similar to that of the regular shape. The ascending CWF is consistent with the negative space charge created by trapped photogenerated electrons under continuous illumination, which induces the ascending transient current, in which CWF damping due to the lifetime is overcome. Moreover, the charge-collection efficiencies at voltage biases of 100 and 300 V are higher in the case of continuous illumination than those in the dark. We interpret this effect as a result of the filling of electron traps by electrons created by steady excitation.

C. Many’s equation

Many’s Eq. (4) is routinely used in the evaluation of the mobility-lifetime product and surface recombination. However, it is seen in Fig. 2 that the fit with Eq. (4) neither approximates the experiment satisfactorily nor gives a value of $\mu_e\tau_e$ as evaluated by alpha spectroscopy. The reason is primarily due to the experimental conditions: space-charge formation significantly violates the homogeneous electric field in the sample presumed in the derivation of Eq. (4). With the aim of assessing this eventuality, we perform the simulation with the DDF model using the defect parameters given in Table I and taking a very low excitation intensity of $I = 2.5 \times 10^9$ photons per cm^2 per second, which is 1000 times less than the maximum intensity used in Fig. 5. Photoinduced space-charge formation is then significantly suppressed. Such a measurement of the photoconductivity is limited only to samples with low noise, so that a good-quality signal can be retrieved. Calculations are performed in the dynamic regime of the photoconductivity measurements, as observed in Fig. 8(a). Both voltage and light are switched on at $t = 0$ for the sample at equilibrium, and the current is obtained after a respective period, t_d , of steady illumination and biasing. The dark current is calculated in the same way, but without switching on the light. This approach ensures well-defined setting of the sample evolution without inevitable memory effects,

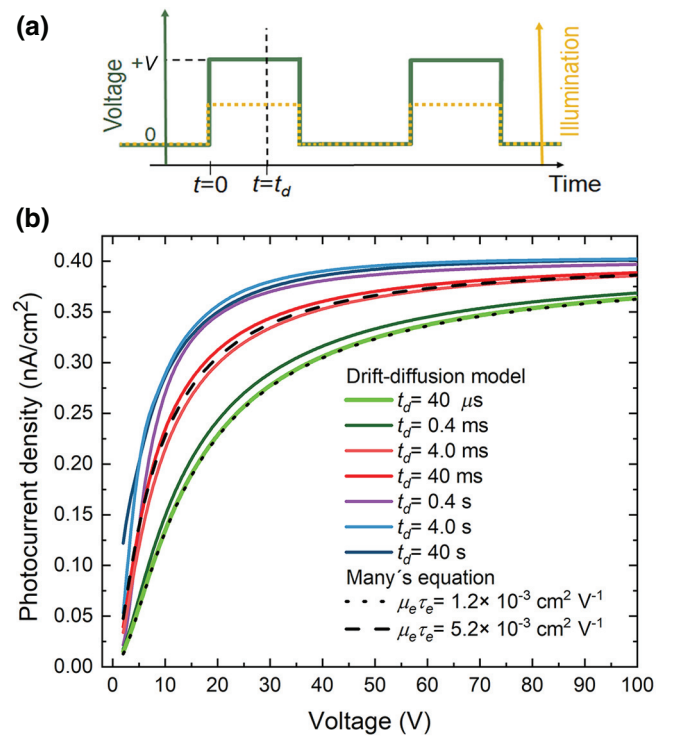


FIG. 8. (a) Time scheme of chopped experiment. (b) DDF model of PV characteristics obtained in a chopped regime of illumination, with different periods, t_d , of illumination and biasing (solid lines), and their comparison with Many’s Eq. (4) (dashed and dotted lines) with various mobility-lifetime products.

which should be anticipated in a real chopped experiment. The photocurrent is obtained by the differentiation of the values. The results are shown in Fig. 8(b), where the PV characteristics for different t_d are plotted. We also add relevant graphs of Many’s Eq. (4) with the correct value of $\mu_e\tau_e = 1.2 \times 10^{-3} \text{ cm}^2/\text{V}$ (dotted line) and a different value of $\mu_e\tau_e = 5.2 \times 10^{-3} \text{ cm}^2/\text{V}$ (dashed line).

An exact value of $\mu_e\tau_e$ may be obtained in the short-pulse setup when $t_d < 40 \mu\text{s}$. This finding is consistent with the LTCT measured at a pulsed voltage [30], where an exact value of $\mu_e\tau_e$ unaffected by the polarization may be determined.

Extending t_d to about 1 ms shows a continuous deviation from the curve to significantly larger values of $\mu_e\tau_e = 5.2 \times 10^{-3} \text{ cm}^2/\text{V}$. The reason for this shift is the detrapping properties of level 3, see Table I, acting as the electron trap. The detrapping time of this level is 1 ms. Using t_d similar to or larger than the detrapping time allows trapped carriers to come into equilibrium with free electrons in the conduction band, and the level becomes invisible in time-resolved experiments. Omitting level 3, remaining levels 1 and 2 are defined as $\mu_e\tau_e = 5.2 \times 10^{-3} \text{ cm}^2/\text{V}$, and a comparison of calculated profiles with the respective (dashed) curve perfectly agrees with this expectation.

A further increase of t_d to $t_d > 0.1$ s shows a continuous deflection of the curve, especially at low voltage, which can be interpreted as a further improvement of $\mu_e \tau_e$. Such an interpretation is, however, incorrect. The correct explanation consists of (i) the charging of deep levels due to electron depletion induced by blocking of the cathode, as defined by low $\gamma_e^{(0)}$, and (ii) in the trapping of photoholes near the cathode. While (i) induces the positive space charge within the bulk of the sample, process (ii) entails the formation of a large positive space charge in a thin layer in the cathode. The activity of both processes leads to an enhancement of the electric field near the cathode and an increase of the photocurrent at low voltage for photoconductive gain.

To conclude, the validity of Many's Eq. (4) is, in practice, limited mainly by three factors. The first is a negative space charge from trapped photoelectrons, which leads to an inhomogeneous electric field profile. The use of Many's Eq. (4) then leads to a significantly lower value of $\mu_e \tau_e$ compared with that of its real value. The second factor corresponds to the case of an experiment in which period t_d is similar to or longer than that of the detrapping time of a shallow level. In this case, the shallow level is not reflected in the PV measurement. As mentioned in Sec. IV A, level 3 does not strongly influence the fitted shape of the PV curves in Fig. 5, where only energy levels 1 and 2 are important in the fit of the photoconductivity. Level 3 is here added according to knowledge of the lifetime obtained from alpha spectroscopy. The third frequent phenomenon limiting the relevance of Many's Eq. (4) is a positive space charge in the vicinity of cathode, which may lead to photoconductive gain. The use of Many's Eq. (4), in the case of the last two phenomena, leads to a significantly higher value of $\mu_e \tau_e$ than that recorded in reality.

D. Space-charge density

Previous studies [7–25] measured the steady-state PV characteristics to evaluate the mobility-lifetime product. However, as we demonstrate in this paper, even for a chopped regime of illumination, with a different period, t_d , of illumination and biasing, correct evaluation of the carrier lifetime is restricted to a sufficiently short period of t_d . Such a short t_d , puts additional demands on laboratory equipment and practically negates the convenience of photoconductivity measurements, which profit from their simplicity. Many's Eq. (4) and du Chatenier's model, therefore, do not allow researchers to credibly determine the mobility-lifetime product or other dynamic parameters. Here, the following question arises: what is the practical use of steady-state or chopped PV characteristics when one of the most crucial material parameters, the carrier lifetime, cannot be determined?

Recent progress in the development of radiation detectors is reflected mainly in a significant increase in a carrier

lifetime. In (Cd,Zn)Te, the mobility-lifetime product and electron lifetime exceed $0.1 \text{ cm}^2/\text{V}$ and $100 \mu\text{s}$, respectively [47]. Contrary to the mastered sufficiently long lifetime, the charging of detectors still remains an issue. Even weak charging at a level of 10^9 cm^{-3} may disable thick detectors, especially those of several centimeters thick, from application. Suppression of space-charge formation in biased semiconductor radiation detectors thus represents an important challenge for further progress in high-quality detector research. The space charge leads to an inhomogeneous electric field distribution inside the material, and it can even induce the appearance of an inactive layer where the electric field falls to almost zero.

As follows from the analysis above, in contrast to the carrier lifetime, which is barely accessible from photoconductivity measurements, space-charge formation in illuminated detectors may be conveniently studied. Previously defined models, SCLP1, SCLP2, and DDF, may be used for the determination of the space-charge distribution within the sample.

Average space-charge density (ρ), depicting the space-charge distribution, can be easily determined by the integration of Gauss's law:

$$\langle \rho \rangle = \frac{\epsilon_0 \epsilon_r}{eL} [E(L) - E(0)]. \quad (16)$$

Electric field values of $E(L)$ and $E(0)$, corresponding to the SCLP1 model, may be simply obtained from Eqs. (6) and (8), respectively. In the case of SCLP2 and DDF models, both quantities are obtained simultaneously upon fitting.

First, we calculate $\langle \rho \rangle$ from the DDF model using the fit of PV measurements plotted in Fig. 5. The resulting $\langle \rho \rangle$, depending on applied voltage, is shown in Fig. 9 by dotted lines. We observe the typical ascending-descending profile of $\langle \rho \rangle$ versus applied voltage. The growth of $\langle \rho \rangle$ at low voltage is mediated by the increasing electric field, which promotes penetration of the space charge from the highly excited surface layer to the sample's interior. The descending part of $\langle \rho \rangle$ appears upon exhaustion of the surface source, when space-charge-induced screening is overcome by the voltage. The electric field increases near the cathode, electrons drift rapidly into the sample's interior, and the mean electron density decreases, which accordingly results in space-charge reduction.

In the next step, we calculate $\langle \rho \rangle$ using the SCLP1 fit of the same data. For the sake of clarity, we plot (dashed line) only the curve for the maximum excitation intensity presented in Fig. 2. The SCLP1 fit produces a significantly different curve from that of the DDF model, with a maximum shifted by 50 V towards lower voltage and reaching about half $\langle \rho \rangle$ in the maximum. Apparently, one can deduce that the SCLP1 fit is unsuitable for the credible determination of $\langle \rho \rangle$.

In an effort to identify the reason for the discrepancy between the fits of the DDF and SCLP1 models, we

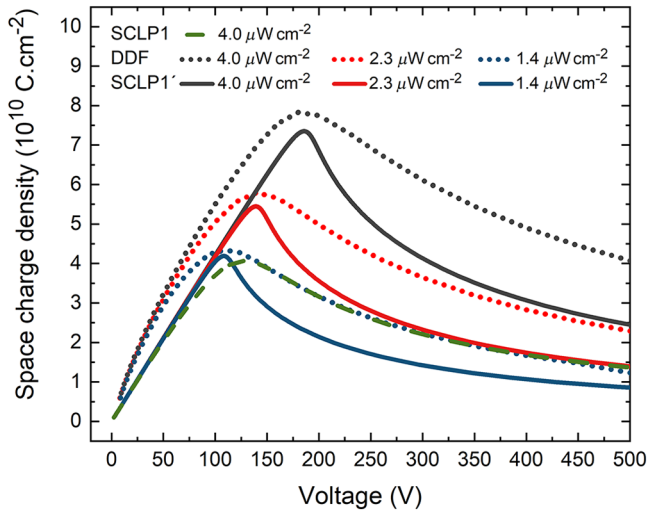


FIG. 9. Average space-charge density $\langle\rho\rangle$ for different illumination intensities. Calculations are performed by using SCLP1 model (green dashed line), DDF model with fit parameters that are the same as those in Fig. 2 (dotted lines), and SCLP1' model with negligible surface recombination (solid line).

concentrate on the shoulder that separates the rising and saturation parts of the PV characteristics. We find that a much better agreement between $\langle\rho\rangle$ calculated from the SCLPs and DDF models is obtained by using a modified SCLP1' fit, which is defined by the position of this shoulder, where only parameter θ is fitted and s is fixed to be very low. The reason for this improvement involves the systematic error embodied in the two-parametric (θ, s) fit of the PV experiment in its ascending part by the oversimplified SCLP1 model. The effort to fit a nearly linear course of the PV curve by the implicitly parabolic-like profile of the SCLP1 model leads to a higher value of s_e and consequently, to a less sharp shoulder in the PV curve. Due to this feature, $\langle\rho\rangle$ derived by the two-parametric fit is lower and its maximum is shifted to lower voltage. Respective $\langle\rho\rangle$ values calculated with the SCLP1' model are plotted as solid lines in Fig. 9. Good agreement with the DDF model, especially at the maxima, is clearly seen.

Summarizing these achievements, we supply practical advice to researchers for how they may determine, easily and with acceptable precision, the average space-charge density from the SCLP1 model. First, one has to determine, as precisely as possible, the position of the shoulder in the PV characteristic, which is defined by voltage V_S and photocurrent density j_S . Parameter θ is then calculated, according to Eq. (1), as

$$\theta = \frac{8}{9} \frac{L^3 j_S}{\varepsilon_0 \varepsilon_s \mu_e V_S^2}. \quad (17)$$

Other quantities, i.e., electric field and space charge, are then calculated from Eqs. (6) and (16), when the boundary

condition in Eq. (8), with low s , typically 10^4 cm/s, is used. Taking the critical fitted point in the photoconductivity shoulder is an optimum option, since it corresponds to the sample with a minimized effect of holes, compensating for the space charge at low voltage and, simultaneously, reduced surface recombination due to the drain of electrons induced by enhanced voltage. In contrast to $\theta = 5 \times 10^{-5}$ determined by the SCLP1 fit in Fig. 2, the improved approach affords $\theta = 2.7 \times 10^{-5}$.

The advantage of this procedure, in contrast to the obvious SCLC technique, lies in the versatility of the SCLP methods applicable to materials equipped with different contacts, either blocking or injecting. Sufficiently intensive illumination overcomes the effect of the contacts and the space charge may be determined independently.

Photoconductivity may also be used in the mapping of the lateral electric field nonuniformity of planar samples, where scanning of the sample's area may be achieved by multiple other techniques. An example of such an investigation is found in Ref. [48].

V. CONCLUSION

Steady-state photocurrents are measured on planar (Cd, Zn)Te radiation detectors under above-band-gap illumination and are theoretically studied by analytical and numerical models. Three models, SCLP1, SCLP2, and the drift-diffusion model, describing space-charge-limited photocurrents, are developed and conveniently applied in the fitting of experimental data with much better precision than that obtained in a previous approach using Many's Eq. (4). Additionally, we create a model that describes transient currents in the case of an inhomogeneous space-charge distribution induced by cathode illumination. Within the SCLP1/SCLP2 models, we show that degeneracy of deep level leads to a slower photocurrent onset, corresponding to a larger polynomial exponent than that of the second power resulting in SCLP1. We conclude that the shape of the onset can be used as a rough estimation of whether shallow or deep levels dominate in the material. Moreover, we propose a simple method for the determination of the average space-charge density from the SCLP1 model at a certain voltage.

The numerical drift-diffusion model explains consistently all experimental data, the PV characteristics at various illumination intensities, and the transient current measured at different biasing in the sample held both in the dark and with a continuously LED illuminated cathode. Three defect levels, with energies of 0.66, 0.85, and 0.50 eV, are ascribed to the measured sample. The experimentally observed linear onset of the photocurrent at low voltages, which also frequently appears in multiple studies, is explained by the compensation of the negative space charge near the illuminated cathode by trapped holes.

Numerical simulations of PV characteristics at low intensities and in the chopped regime show that the validity of Many's Eq. (4) is, in practice, limited not only by the space charge from trapped photogenerated electrons, but also by the photoconductive gain caused by trapping of photogenerated holes in the vicinity of the cathode. An incorrect determination of the mobility-lifetime product also results from the fact that shallow levels, with detrapping times shorter than the period of illumination, do not influence PV characteristics.

These achievements allow us to conclude that the measurement of steady-state photocurrents, if it involves a single analytical method, does not enable researchers to evaluate the carrier lifetime and other dynamic carrier parameters. The measurement of PV characteristics should be complemented by the independent measurement of the mobility-lifetime product, such as the transient current technique or alpha-spectroscopy measurements. The measurement of PV characteristics at various intensities, together with knowledge of the carrier lifetime, then gives a detailed picture of the defect structure of the material using the drift-diffusion model. Certain shallow levels may not be distinguished in the defect structure from PV measurements without considering the lifetime obtained from other experiments.

ACKNOWLEDGMENTS

This project is financially supported by the Grant Agency of the Czech Republic under Grant No. P102/18-12449S, the Grant Agency of Charles University under Grant No. 1374218, and Charles University under Grant No. SVV-2019-260445.

APPENDIX

In the SCLP2 model, the Fermi-Dirac statistics must be used to describe the occupancy of the deep trap level. Thus, the concentration of trapped electrons may be expressed as $n_t = N_t/(1 + n_1/n)$, with the parameter $n_1 = N_c \exp[E_t/(kT)]$ being related to the trap-level position. Considering also the dark concentration of free electrons, n_0 , and trapped electrons, n_{t0} , the Gauss law may be used in the form

$$\frac{dE}{dx} = -\frac{e}{\epsilon_0 \epsilon_r} \left(-\frac{j}{e \mu_e E} + \frac{N_t}{1 - \frac{n_1 e \mu_e E}{j}} - n_0 - \frac{N_t n_0}{n_0 + n_1} \right). \quad (\text{A1})$$

By converting the bracket in Eq. (A1) to a common denominator, we get the second-order polynomial in $E(x)$ in the numerator. If we mark E_1 and E_2 as the roots of the

polynomial, Eq. (A1) then attains the form

$$\frac{E \left(1 - \frac{n_1 e \mu_e E}{j} \right)}{(E - E_1)(E - E_2)} dE = -\frac{1}{\epsilon_0 \epsilon_r \mu (n_0 + n_1)} dx. \quad (\text{A2})$$

Corresponding roots E_1 and E_2 are

$$E_{1,2} = \frac{n_1 + N_t - D \pm \sqrt{(D - n_1 - N_t)^2 + 4n_1 D}}{-2AD}, \quad (\text{A3})$$

where parameters A and D are defined in Eq. (A4).

The semianalytical SCLP2 model given by Eq. (14) is obtained by applying partial fraction decomposition to the integrand on the left side of Eq. (A2) followed by partial integration. All parameters E_1 , E_2 , A , B , C , and D , appearing in Eq. (14), are listed in Eq. (A3) and in the following:

$$A = \frac{n_1 e \mu_e}{j}, \quad B = \frac{E_1(1 - AE_1)}{E_1 - E_2}, a) \quad (\text{A4a})$$

$$C = \frac{E_2(1 - AE_2)}{E_2 - E_1}, \quad D = n_0 + \frac{N_t n_0}{n_0 + n_1}. b) \quad (\text{A4b})$$

The boundary condition for the SCLP2 model,

$$E(0) = \frac{1}{2e \mu_e n_0} \times \left[e(I_l + n_0 s_e) - j - \sqrt{4ej n_0 s_e + (eI_l - j + en_0 s_e)^2} \right] \quad (\text{A5})$$

is attained from the balanced equation involving the dark current and electron density:

$$I_l - s_e(n - n_0) - \frac{j - j_d}{e} = 0. \quad (\text{A6})$$

A generalization to the multiple-level design cannot be easily introduced here, since the roots of the respective polynomials appearing in Eq. (A2) cannot be calculated analytically. Nevertheless, the direct numerical integration of Eq. (A1) does not cause considerable problems.

-
- [1] M. Lampert, Simplified theory of space-charge-limited currents in an insulator with traps, *Phys. Rev.* **103**, 1648 (1956).
 - [2] N. F. Mott and R. W. Gurney, *Electronic Processes in Ionic Crystals*, 2nd Ed. (Dover Publications Inc., New York, 1964).
 - [3] J. A. Röhr, D. Moia, S. A. Haque, T. Kirchartz, and J. Nelson, Exploring the validity and limitations of the mott-gurney law for charge-carrier mobility determination of

- semiconducting thin-films, *J. Phys. Condens. Matter* **30**, 13 (IOP Publishing, 2018).
- [4] C. Manfredotti, A. Rizzo, L. Vasanelli, S. Galassini, and L. Ruggiero, Electron trapping levels in cadmium selenide single crystals, *J. Appl. Phys.* **44**, 5463 (1973).
- [5] M. Ayoub, M. Hage-Ali, J. M. Koebel, R. Regal, C. Rit, F. Klotz, A. Zumbiehli, and P. Siffert, Real defect concentration measurements of nuclear detector materials by the combination of PICTS and SCLC methods, *Mater. Sci. Eng. B Solid-State Mater. Adv. Technol.* **83**, 173 (2001).
- [6] A. Many, High-Field effects in photoconducting cadmium sulphide, *J. Phys. Chem. Solids* **26**, 575 (1965).
- [7] Y. Cui, M. Groza, D. Hillman, A. Burger, and R. B. James, Study of surface recombination velocity of CdZnTe radiation detectors by direct current photoconductivity, *J. Appl. Phys.* **92**, 2556 (2002).
- [8] Y. Cui, G. W. Wright, X. Ma, K. Chattopadhyay, R. B. James, and A. Burger, DC photoconductivity study of semi-insulating CdZnTe crystals, *J. Electron. Mater.* **30**, 774 (2001).
- [9] Y. Ling, J. Min, X. Liang, J. Zhang, L. Yang, Y. Zhang, M. Li, Z. Liu, and L. Wang, Carrier transport performance of CdZnTe detector by direct current photoconductive technology, *J. Appl. Phys.* **121**, 034502 (2017).
- [10] M. Zanichelli, M. Pavesi, A. Zappettini, L. Marchini, N. Auricchio, E. Caroli, and M. Manfredi, Characterization of bulk and surface transport mechanisms by means of the photocurrent technique, *IEEE Trans. Nucl. Sci.* **56**, 3591 (2009).
- [11] Y. Cui, M. Groza, G. W. Wright, U. N. Roy, A. Burger, L. Li, F. Lu, M. A. Black, and R. B. James, Characterization of Cd_{1-x}Zn_xTe crystals grown from a modified vertical bridgman technique, *J. Electron. Mater.* **35**, 1267 (2006).
- [12] L. Bao, G. Zha, B. Zhang, J. Dong, Y. Li, and W. Jie, Investigation of neutron irradiation effects on the properties of Au/CdZnTe junction, *Vacuum* **167**, 340 (Elsevier, 2019).
- [13] Z. Burshtein, J. K. Akujieze, and E. Silberman, Carrier surface generation and recombination effects in photoconduction of HgI₂ single crystals, *J. Appl. Phys.* **60**, 3182 (1986).
- [14] A. Levi, M. M. Schieber, and Z. Burshtein, Carrier surface recombination in HgI₂ photon detectors, *J. Appl. Phys.* **54**, 2472 (1983).
- [15] S. Wang, Z. Liu, J. A. Peters, M. Sebastian, S. L. Nguyen, C. D. Malliakas, C. C. Stoumpos, J. Im, A. J. Freeman *et al.*, Crystal growth of Tl₄CdI₆: A wide band Gap semiconductor for hard radiation detection, *Cryst. Growth Des.* **14**, 2401 (2014).
- [16] A. C. Wibowo, C. D. Malliakas, Z. Liu, J. A. Peters, M. Sebastian, D. Y. Chung, B. W. Wessels, and M. G. Kanatzidis, Photoconductivity in the chalcogenide semiconductor, SbSeI: A New candidate for hard radiation detection, *Inorg. Chem.* **52**, 7045 (2013).
- [17] S. L. Nguyen, C. D. Malliakas, J. A. Peters, Z. Liu, J. Im, L. Zhao, M. Sebastian, H. Jin, H. Li *et al.*, Photoconductivity in Tl₆Si₄: A novel semiconductor for hard radiation detection, *Chem. Mater.* **25**, 2868 (2013).
- [18] S. M. Islam, S. Vanishri, H. Li, C. C. Stoumpos, J. A. Peters, M. Sebastian, Z. Liu, S. Wang, A. S. Haynes *et al.*, Cs₂Hg₃H₄: A Low-dimensional direct bandgap semiconductor, *Chem. Mater.* **27**, 370 (2015).
- [19] S. J. Grenadier, A. Maity, J. Li, J. Y. Lin, and H. X. Jiang, Origin and roles of oxygen impurities in hexagonal boron nitride epilayers, *Appl. Phys. Lett.* **112**, 162103 (2018).
- [20] K. Ahmed, R. Dahal, A. Wetz, J. J. Lu, Y. Danon, and I. B. Bhat, Solid-state neutron detectors based on thickness scalable hexagonal boron nitride, *Appl. Phys. Lett.* **110**, 023503 (2017).
- [21] A. Maity, S. J. Grenadier, J. Li, J. Y. Lin, and H. X. Jiang, Hexagonal boron nitride neutron detectors with high detection efficiencies, *J. Appl. Phys.* **123**, 044501 (2018).
- [22] A. Maity, S. J. Grenadier, J. Li, J. Y. Lin, and H. X. Jiang, Toward achieving flexible and high sensitivity hexagonal boron nitride neutron detectors, *Appl. Phys. Lett.* **111**, 033507 (2018).
- [23] A. Maity, S. J. Grenadier, J. Li, J. Y. Lin, and H. X. Jiang, High sensitivity hexagonal boron nitride lateral neutron detectors, *Appl. Phys. Lett.* **114**, 222102 (2019).
- [24] W. Zheng, R. Lin, Z. Zhang, Q. Liao, J. Liu, and F. Huang, An ultrafast-temporally-responsive flexible photodetector with high sensitivity based on high-crystallinity organic-inorganic perovskite nanoflake, *Nanoscale* **9**, 12718 (2017).
- [25] Z. Yang, M. Wang, H. Qiu, X. Yao, X. Lao, S. Xu, Z. Lin, L. Sun, and J. Shao, Engineering the exciton dissociation in quantum-confined 2D CsPbBr₃ nanosheet films, *Adv. Funct. Mater.* **28**, 1705908 (2018).
- [26] F. J. du Chatenier, Space-charge-limited photocurrent in vapour-deposited layers of red lead monoxide, *Philips Res. Rep.* **23**, 142 (1968).
- [27] M. Pavesi, A. Santi, M. Bettelli, A. Zappettini, and M. Zanichelli, Electric field reconstruction and transport parameter evaluation in CZT X-Ray detectors, *IEEE Trans. Nucl. Sci.* **64**, 2706 (2017).
- [28] H. Li, C. D. Malliakas, J. A. Peters, Z. Liu, J. Im, H. Jin, C. D. Morris, L. Zhao, B. W. Wessels *et al.*, Cscdq₃ (Q = Se, Te): New photoconductive compounds As potential materials for hard radiation detection, *Chem. Mater.* **25**, 2089 (2013).
- [29] P. Praus, E. Belas, J. Bok, R. Grill, and J. Pekárek, Laser induced transient current pulse shape formation in (CdZn)Te detectors, *IEEE Trans. Nucl. Sci.* **63**, 246 (2016).
- [30] A. Musiienko, R. Grill, E. Belas, P. Praus, J. Pipek, and H. Elhadidy, Characterization of polarizing semiconductor radiation detectors by laser-induced transient currents, *Appl. Phys. Lett.* **111**, 8 (2017).
- [31] S. Del Sordo, L. Abbene, E. Caroli, A. M. Mancini, A. Zappettini, and P. Ubertini, Progress in the development of CdTe and CdZnTe semiconductor radiation detectors for astrophysical and medical applications, *Sensors* **9**, 3491 (2009).
- [32] P. N. Murgatroyd, Theory of space-charge-limited current enhanced by frenkel effect, *J. Phys. D. Appl. Phys.* **3**, 151 (1970).
- [33] The original work [26] is performed on a *p*-type material with anode illumination and a value of *p*/*τ* is also reported.
- [34] K. Suzuki, T. Sawada, and K. Imai, Effect of DC bias field on the time-of-flight current waveforms of CdTe and CdZnTe detectors, *IEEE Trans. Nucl. Sci.* **58**, 1958 (2011).

- [35] M. Zanichelli, A. Santi, and A. Zappettini, Charge collection in semi-insulator radiation detectors in the presence of a linear decreasing electric field, *J. Phys. D: Appl. Phys.* **46**, 365103 (2013).
- [36] A. Santi, M. Zanichelli, G. Piacentini, M. Pavesi, A. Cola, and I. Farella, An original method to evaluate the transport parameters and reconstruct the electric field in solid-state photodetectors, *Appl. Phys. Lett.* **104**, 193503 (2014).
- [37] Š Uxa, E. Belas, R. Grill, P. Praus, and R. B. James, Determination of electric-field profile in CdTe and CdZnTe detectors using transient-current technique, *IEEE Trans. Nucl. Sci.* **59**, 2402 (2012).
- [38] G. Cavalleri, E. Fabri, E. Gatti, and V. Svelto, On the induced charge in semiconductor detectors, *Nucl. Instruments Methods* **21**, 177 (1963).
- [39] R. Grill, E. Belas, J. Franc, M. Bugár, Š Uxa, P. Moravec, and P. Höschl, Polarization study of defect structure of CdTe radiation detectors, *IEEE Trans. Nucl. Sci.* **58**, 3172 (2011).
- [40] M. Lavagna, J. P. Pique, and Y. Marfaing, Theoretical analysis of the quantum photoelectric yield in schottky diodes, *Solid State Electron.* **20**, 235 (1977).
- [41] D. Gutkowitz-Krusin, On the carrier collection efficiency of amorphous silicon hydride schottky barrier solar cells: Effects of recombination, *J. Appl. Phys.* **52**, 5370 (1981).
- [42] P. Praus, E. Belas, J. Franc, R. Grill, P. Höschl, and J. Pekárek, Electronic pulse shape formation in transient charge and transient current detection approach in (CdZn)Te detectors, *IEEE Trans. Nucl. Sci.* **61**, 2333 (2014).
- [43] S. F. Soares, Photoconductive gain in a schottky barrier photodiode, *Jpn. J. Appl. Phys.* **31**, 210 (1992).
- [44] D. Kranzer, Mobility of holes of zinc-blende III-V and II-VI compounds, *Phys. Status Solidi* **26**, 11 (1974).
- [45] P. Horodyský and P. Hlídek, Free-exciton absorption in bulk CdTe: Temperature dependence, *Phys. Status Solidi Basic Res.* **243**, 494 (2006).
- [46] J. Franc, V. Dědič, M. Rejhon, J. Zázvorka, P. Praus, J. Touš, and P. J. Sellin, Control of electric field in CdZnTe radiation detectors by above-bandgap light, *J. Appl. Phys.* **117**, 165702 (2015).
- [47] A. E. Bolotnikov, G. S. Camarda, E. Chen, R. Gul, V. Dedic, G. Geronimo, J. Fried, A. Hossain, J. M. MacKenzie, and L. Ocampo, Use of the drift-time method to measure the electron lifetime in long-drift-length CdZnTe detectors, *J. Appl. Phys.* **120**, 104507 (2016).
- [48] J. Zázvorka, J. Pekárek, R. Grill, E. Belas, K. Ridzoňová, J. Pipek, and J. Franc, Inhomogenous resistivity and its effect on CdZnTe-based radiation detectors operating at high radiation fluxes, *J. Phys. D:Appl. Phys.* **52**, 325109 (2019).